Chinese Chemical Letters 34 (2023) 107946

Contents lists available at ScienceDirect

Chinese Chemical Letters

journal homepage: www.elsevier.com/locate/cclet

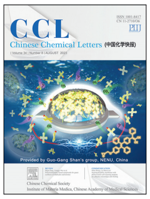

Self-swelling derived frameworks with rigidity and flexibility enabling high-reversible silicon anodes

Peng Liu[a], Bingqing Li[a], Jianli Zhang[b], Hongfu Jiang[b], Zhong Su[a,*], Chao Lai[a,*]

[a] *School of Chemistry and Materials Science, Jiangsu Normal University, Xuzhou 221116, China*
[b] *Jiangsu Xinhua Semiconductor Material Technology Co., Ltd., Xuzhou 221116, China*

ARTICLE INFO

Article history:
Received 8 September 2022
Revised 10 October 2022
Accepted 24 October 2022
Available online 29 October 2022

Keywords:
Self-swelling derived framework
High mass loading
High areal capacity
Si anodes
Free-binder

ABSTRACT

Silicon is recognized as the most advantageous next-generation anode material for LIBs in terms of its extremely high theoretical capacity and appropriate operating voltage. However, the application of Si anode is limited by huge volume expansion emerging with cycling, which in turn induces the collapse of the electrode structure, resulting in rapid capacity decay. Here, we report a strategy using self-swelling artificial laponite to prepare a laponite/MXene/CNT composite framework with both rigidity and flexibility, which can excellently address these challenges of Si anode. The self-swelling artificial laponite participates in the construction of hierarchical and porous structures, providing sufficient buffer space to mitigate the volume expansion of the Li_xSi alloying reaction. Meanwhile, tough and tightly cross-linked silicate nanosheets can improve the mechanical strength of the framework for strong structural stability. More importantly, the negative charge between the layers of artificial laponite can effectively promote fast Li-ion transport in the electrode. This free-standing silicon anode enables the preparation of high areal capacity electrodes to further enhance the energy density of LIBs and a higher reversible capacity of 2381.8 mAh/g at 0.1 C after 50 cycles with an initial coulombic of 85.6%. This work provides a simple and practical fabrication strategy for developing high-performance Si-based batteries, which can speed up their commercialization.

The constant development of Lithium-ion batteries (LIBs) is critically significant for portable electronics, electric vehicles, and renewable large-scale grid applications [1–4]. Traditional graphite anodes in LIBs, on the other hand, are approaching their theoretical capacity limit of 372 mAh/g, which is insufficient to meet the social demands of big energy storage systems [5–7]. Towards this focus, the current priority is to exploit the electrode materials with greater energy storage ability and high theoretical capacity [8–10]. Among the potential candidates, Silicon (Si) is extensively utilized as an ideal anode material for LIBs, owing to its large theoretical capacity (4200 mAh/g), low cost, and environmental friendliness [11–14]. However, before commercializing Si anodes, some critical internal issues must be resolved. Specifically, the massive volume fluctuations (>300%) that occur during repetitive cycling cause the electrode structure to collapse, resulting in rapid capacity deterioration [15–17]. Also, the poor electrical conductivity of Si nanoparticles seriously affects the kinetic processes of electrochemical reaction [16,18], limiting their use in fast-charging devices.

Recent studies focusing on the challenges of Si anode showed that the stability of electrode structure was especially critical and a three-dimensional (3D) free-standing framework is defined as an ideal material for stabilizing the volume expansion of the Li-Si alloying reaction [19–23]. This free-standing architecture can not only possess controllable structural adjustability to load Si nanoparticles and alleviate the structural strain caused by repeated Li_xSi alloying reaction processes, but also provide large electrochemical reaction interfaces and shortened paths for rapid Li^+ ions and electrons diffusion [23–25]. For example, the design of architecture electrode was successfully reported using two-dimensional (2D) graphene and One-dimensional (1D) carbon nanotubes to form a 3D framework as the conductive scaffold for Si active material [26–28]. Besides, carbon nanocage is also successfully prepared as a host for Si anode by calcining templates, such as sponges [29] and aerogels [30,31] and performing rigorous acid washing. Although these 3D frameworks with optimized encapsulation and porosity can enhance the ions and electrons transport kinetics, however, the procedure of industrial production is seriously restricted due to the complexity of the electrode preparation. Thus, a facile and general method for preparing 3D frameworks to host

---

* Corresponding authors.
E-mail addresses: suzhongjs@163.com (Z. Su), laichao@jsnu.edu.cn (C. Lai).

https://doi.org/10.1016/j.cclet.2022.107946

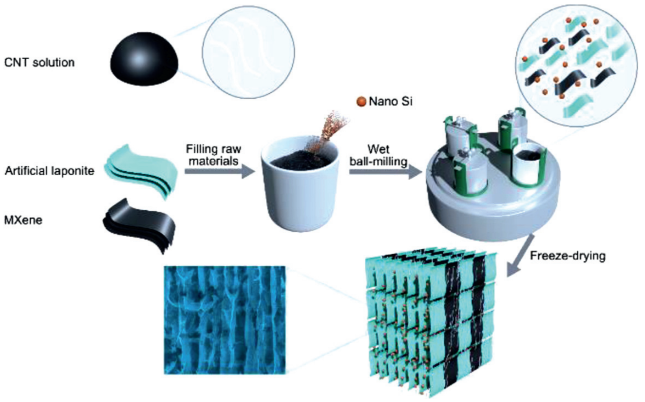

Scheme 1. The schematic diagram of the preparation of the 3D Si anode.

Si urgently needs to be developed to speed up their commercial application.

Herein, we proposed a brand-new strategy to build 3D-ordered interconnected skeletons as a substrate for achieving Si loading based on the self-swelling material, artificial laponite (A-Lap, $Li_2Mg_2O_9Si_3$). As shown in Scheme 1, First, A-Lap was added to Water-based conductive paste (CNT solution and MXene), then Nano Si was added and uniformly blended by wet ball milling. When in contact with water, the repulsive force between the A-Lap layer is significantly enhanced due to the interaction of charged groups in the A-Lap layer, and the stacked structures swell into nanosheets under the action of electrostatic repulsion [32]. Next, the slurry was cast on the current collector and freeze-dried. The disordered 2D nanosheets and 1D nanotube were driven into ordered 3D layered structures by utilizing the directional growth of ice crystals. The interwoven stacking of CNT, MXene and A-Lap sheets builds a flexible 3D framework and retains sufficient pores to achieve Si encapsulation. The homogeneous distribution of Si nanoparticles, wide porosity, and adjustable structural flexibility of this self-assembled 3D skeleton structure make it ideal for stable long-term cycling of electrochemical reactions. Furthermore, the design of controllable electrode thickness and mass loading is crucial for translating the high energy density output achieved by Si active materials into commercial application.

SEM and TEM imaging were performed to characterize the A-Lap in detail before and after swelling. After self-swelling in water, A-Lap undergoes a clear morphological shift from bulk to lamellar structure (Figs. 1a-c). In addition, the thickness and size of A-Lap nanosheets were further determined by AFM images, corresponding to 3.5 nm and 9 µm, respectively (Figs. 1d and e). Following that, a zeta-potentiometer result revealed that A-Lap had a net negative charge, as shown in (Fig. S1 in Supporting information). Furthermore, the negative charge between the layers can effectively pair with Li-ions, allowing for rapid transport in the electrode. To evaluate the chemical valence of A-Lap before and after swelling, X-ray photoelectron spectroscopy (XPS) of elemental Si is also provided. The entire Si 2p spectrum eventually moved to high energy, as shown in Fig. 1f, with an extra peak of Si-OH at 103.5 eV in the swollen A-Lap, showing that hydroxyl groups in water are adsorbed on the surface of the A-Lap layers [33,34]. The structural evolution of A-Lap from bulk to layer was further characterized by XRD and FTIR spectra. It was found that all the obvious diffraction peaks of the A-Lap layer disappeared and the obvious weakened Si-O and Mg-O peaks of the A-Lap layer were found compared to bulk A-Lap (Figs. S2 and S3 in Supporting information), indicating an increase in interlayer spacing after swelling [32]. Considering the thickening, thixotropic, and strong adsorption ability of A-Lap during the swelling process, we further evaluated the rheological behavior of CNT/MXene slurry and A-Lap/CNT/MXene slurry (Fig. 1g and Fig. S4 in Supporting information). Both samples exhibited non-Newtonian characteristics and shear-thinning behavior, and the viscosity decreased with increasing shear rate. Due to the aggregates formed by the cross-linking of A-Lap swollen nanosheets, the viscosity is obviously raised [35]. Interestingly, A-Lap/CNT/MXene slurry showed higher viscosity at any shear rate and was enhanced by a factor of nearly 5 at static (Fig. 1g). Such

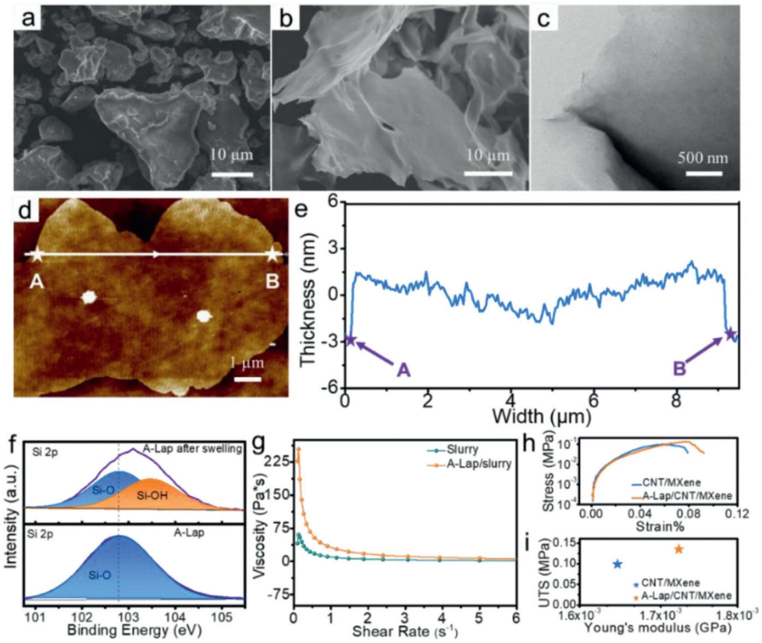

Fig. 1. (a) SEM images of the A-Lap before swelling and (b) after swelling. (c) TEM image of the A-Lap after swelling. (d, e) AFM image and height profile of A-Lap after swelling. (f) Si 2p XPS pattern of the A-Lap before and after swelling. (g) Rheological properties of the conductive paste, viscosity plotted as a function of shear rate. (h) The stress (i.e. tensile energy density required to break film) is plotted as a function of strain at break (%). (i) Tensile strength plotted as a function of Young's modulus. After adding A-Lap, the mechanical properties indicated enhanced toughness and tensile strength.

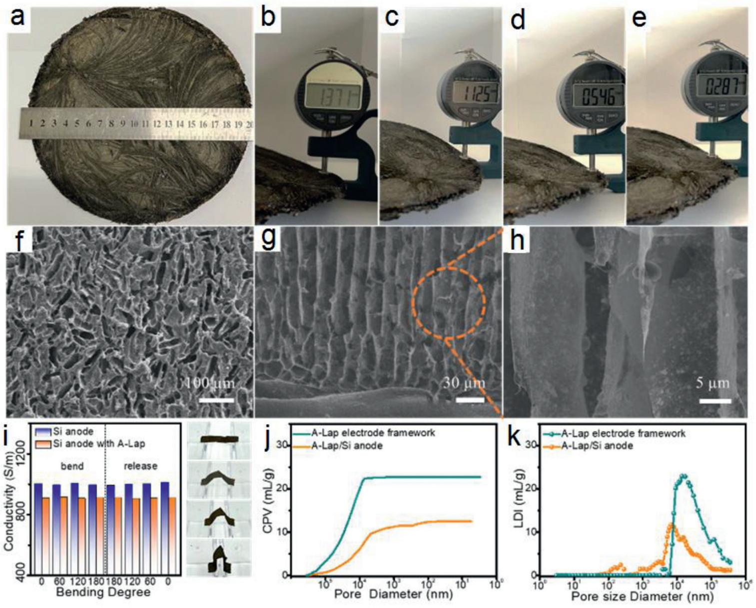

Fig. 2. (a) The photograph of the 3D Si anode prepared in the laboratory. It showed a diameter close to 20 cm. (b-e) Photographs of the thickness of the silicon anode under different pressures. The electrode thickness can be regulated by applying different pressures without changing the areal loading. (f) The SEM image of the surface of Si anode. (g, h) SEM photos of Si anode in cross-section. The nano Si was well attached to the lamellae, as shown by the magnified view of (g). (i) Electrical conductivity change of the 3D Si anode upon bending, as shown in the inserts. The slightly changing conductivity values indicated the stability of our Si anode. (j, k) The graphs of mercury intrusion experiments were used to analyze the pore volume and pore size distribution.

excellent viscosity helps to allow higher loadings, stabilize the electrode structure, and relieve volumetric strain during the charge and discharge process. Stress-strain curves depicting the tensile toughness and young's modulus were used to demonstrate the mechanical reinforcement supplied by A-Lap (Figs. 1h and i). As anticipated, the framework with A-Lap demonstrated higher mechanical capabilities, allowing for improved electrode stability and crack resistance.

The ability to make 3D Si anodes using self-swelling materials has opened the door to commercialization of 3D electrodes. As shown in Fig. 2a, large-scale preparation was possible even in the laboratory. Additionally, as illustrated in Figs. 2b-e, electrodes of varied thicknesses can be made easily by pressing with controlled pressure. The electrode structure will not collapse even at 1.5 MPa (Fig. S5 in Supporting information). Such a robust electrode structure can be attributed to the excellent mechanical strength of the A-Lap. State of the art technologies including the SEM and elemental mapping strategy showed the porous structure of the Si anode, and it was seen that the Si nanoparticles were uniformly scattered in the skeletal structure (Figs. 2f-h and Fig. S6 in Supporting information), allowing for high loading. Although the conductivity was slightly reduced after adding A-Lap, the flexibility of the electrode was preserved (Fig. 2i). Besides, mercury intrusion experiments were used to analyze the pore volume and pore size distribution (Figs. 2j and k, Table S1 in Supporting information). After encapsulating the nano Si, additional pores were still preserved for Li^+ rapid diffusion channels. These unique 3D Si electrodes combined adjustable thickness, mechanical flexibility, and rapid Li^+ migration, holding great promise for flexible electronics with high energy density.

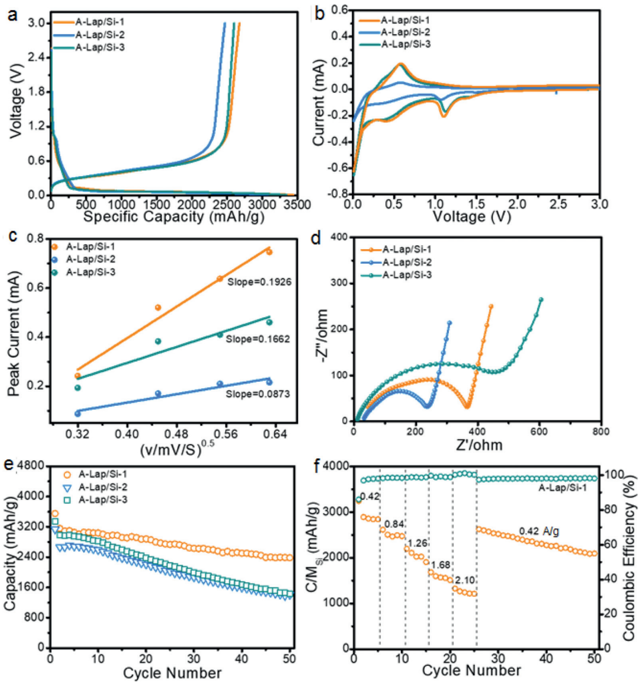

Fig. 3. (a) The first charge-discharge curves of the 3D Si anodes with different contents of A-Lap. (b) The CV curves of the 3D Si anodes with different contents of A-Lap. (c) Linear fitting of the square root of the scanning rates ($v^{0.5}$) *vs.* the peak currents (I_p). The slope is the Li-ion diffusion coefficient. (d) The EIS curves of the 3D Si anodes with different contents of A-Lap before cycling. (e) The long cycle performance of the 3D Si anodes with different contents of A-Lap at 0.1 C. (f) The rate performance of A-Lap/Si-1.

To define the optimal ratio of electrode composition, three different ratios of Si, A-lap, and CNT@MXene are prepared, corresponding to 6:2:2, 6:1:3 and 6:3:1, respectively (labeled as A-lap/Si-1, A-lap/Si-2 and A-lap/Si-3). Their electrochemical performance was also investigated in the 0.01–3 V voltage range [36–38]. Fig. 3a showed the initial charge-discharge curve of the prepared electrode at 0.1 C, which was similar to the typical Li_xSi alloying reaction [39]. Such that the A-lap/Si-1 exhibited a higher specific discharge capacity of 3549.2 mAh/g, accompanied by an initial coulombic efficiency of 85.6%. In addition to the electrochemical performance the lithiation/delithiation behavior of Si anodes was further studied using cyclic voltammetry (CV) curves (Fig. 3b). Cathodic peaks around 0.012 V corresponded to the Li-alloy reaction of Si, and anodic peaks around 0.57 V correspond to the dealloying reaction of Li_xSi [40].

As shown in Fig. 3b and Fig. S8 (Supporting information), the peak around 1.07 V is related to SEI production and disappears in subsequent cycles [41]. As expected, A-lap/Si-1 showed the sharpest peaks and largest curve area, which meant the excellent Li migration kinetics and in-depth Li_xSi alloying/dealloying reaction of the Si anode. Fig. 3c showed the Li-ions diffusion coefficient (D) and was calculated by using the Randles−Sevcik equation (Fig. 3c and Fig. S7 in Supporting information) [42].

$$I_p = 0.4663nF\sqrt{\frac{nFD}{RT}}SC\sqrt{v} \tag{1}$$

The magnitude of the I_p (peak current) can be determined from the CV curve, where n is the number of electrons transferred in the redox reaction, F is the Faraday constant, R is the gas thermodynamic constant, T is the test temperature, S is the contact area between the electrode and the electrolyte, C is the concentration of Li-ions in the electrolyte (1 mol/L), and v is the scanning rate of CV curves. Since the above are all constants or known quantities, Eq. 1 can be rewritten as:

$$I_p = \alpha\sqrt{D}\sqrt{v} \tag{2}$$

By comparing the slopes, the result of A-lap/Si-1 showed the best diffusion coefficient (Table S2 in Supporting information). However, when the addition amounts of A-Lap were further increased, the diffusion rate of the Si anode decreased. This was due to the insulating properties of A-Lap, which led to an increase in impedance, resulting in hindering charge transfer and ion diffusion migration (Fig. 3d). And the electrical conductivity of free-standing 3D Si anodes with different slurry components has been tested. A-Lap/Si-1, A-Lap/Si-2, and A-Lap/Si-3 correspond to 910, 981 and 857 S/m, respectively, which also confirmed that insulated A-Lap will increase resistance (Fig. S7). Meanwhile, the EIS data of A-Lap/Si-1, A-Lap/Si-2 and A-Lap/Si-3 after cycling have been tested. Because of the activation process of electrodes, Si anodes demonstrated smaller semicircles after cycling, and A-Lap/Si-1 exhibited the smallest semicircle, which indicated that the A-Lap/Si-1 electrode had the lowest interfacial resistance after cycling (Fig. S9 in Supporting information) [43,44]. In comparison to A-lap/Si-2 and A-lap/Si-3, A-lap/Si-1 showed the best results, with 2381.8 mAh/g after 50 cycles at 0.1 C (Fig. 3e). A-Lap was only involved in the construction of the 3D framework, for the pristine A-Lap supplied ~50 mAh/g capacity contribution (Fig. S10 in Supporting information). Moreover, the rate performance of A-lap/Si-1 was further studied, as shown in Fig. 3f. It was found that the higher discharge capacities of 3242.3, 2614.1, 2195.9, 1683.8 and 1325.6 mAh/g can be achieved at 0.42, 0.84, 1.26, 1.68 and 2.1 A/g, Also, when the rate returned to 0.42 A/g, a high and reversible discharge capacity of 2091.7 mAh/g was achieved after 50 cycles (Fig. 3f).

Traditional electrodes are limited to the achievable thickness resulting in a low areal capacity (typically, < 4 mAh/cm^2), restricting the energy density of LIBs [45]. However, the great mechanical strength of the A-Lap allowed preparing of thicker electrodes with higher mass loadings and is linearly related to the thickness (Fig. 4a), attaining higher energy density. Also, the extremely high areal capacities scale linearly with mass loading over the entire thickness range (Fig. 4b). Based on these, the A-Lap/Si-1 anodes with different loading from 2 mg/cm^2 to 6.3 mg/cm^2 were prepared to study their electrochemical characterization. The areal capacities were improved from 4.6 mAh/cm^2 to 13.5 mAh/cm^2 on the initial charge-discharge curves (1/20 C rate) (Fig. 4c), agreeing quite well with Fig. 4b and further suggesting a high initial coulombic efficiency (77.8%–80.9%, Fig. S11 in Supporting information). The cycling stabilities of the A-Lap/Si-1 anode with various mass loadings were studied at 1/20 C (Fig. 4d). With low-medium mass loadings, the A-Lap/Si-1 anode achieves extremely stable capacities. For example, the capacity in the 2.43 mg/cm^2 is 2.5 mAh/cm^2 after 50 cycles. Even with large mass loadings of 5–6 mg/cm^2, capacity degradation was rather prevalent (Fig. 4d); owing to the appropriate pore volume and robust layered structure, which prevented the Si anode from breaking during repeated cycling. Though XRD and SEM showed the pulverization of nano Si, the powdered silicon was still contained within the 3D structure and so remains available to store charge (Figs. S12 and S13 in Supporting information). The porosity of Si anodes reduced at high pressure and the stacked lamellar structure became more compact. However, due to the good mechanical performance of A-Lap, the porous 3D structure was not damaged. (Figs. S5 and S14 in Supporting information). So, we applied varied pressures with A-Lap/Si-1 anodes of loading of 4.05 mg/cm^2 and yielded various thicknesses electrodes. Meanwhile, the volumetric energy density was also tested. Although the capacity fades slightly faster, the volumetric energy density increases significantly (Figs. 4e and f). Therefore, this 3D Si anode had great potential in the fabrication of microelectronic devices with high energy density.

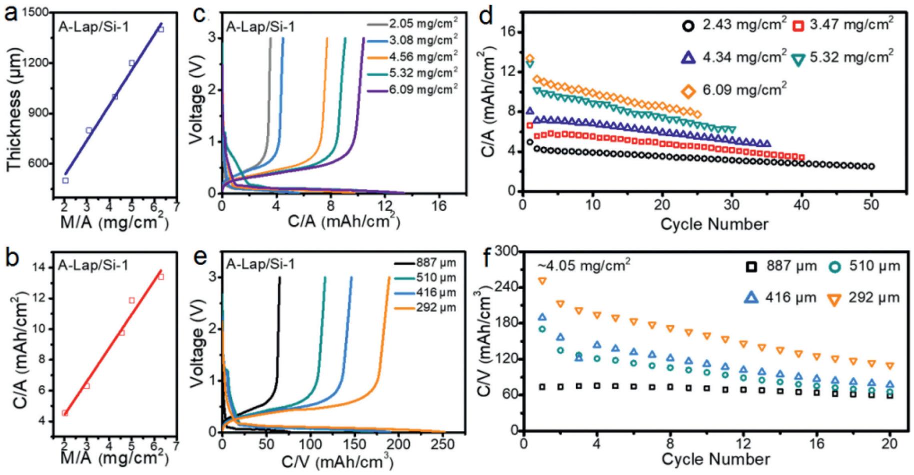

Fig. 4. (a) Electrode coating thickness as a function of electrode mass loading. (b) Electrode area capacity as a function of electrode mass loading. (c) Initial charge-discharge curves showing the areal capacity of 3D Si anodes with mass loadings ranging from 2.05 mg/cm^2 to 6.09 mg/cm^2 at a rate of 1/20 C. (d) Cycling performance representing areal capacity of the 3D Si anodes with different mass loading at the rate of 1/20 C. (e) The initial charge-discharge curves presenting volume capacity of 3D Si anodes at the rate of 1/20 C. (f) Cycling performance indicating volume capacity of the 3D Si anodes with the loading of 4.05 mg/cm^2 at the rate of 1/20 C and electrodes with varied thicknesses were created by applying different pressures.

To summarize, a general method has been specially developed for Si anodes in coping with their unstable electrode structures by using self-swelling materials to build the free-standing 3D framework in one-step. Long-term structural chalking and poor ion conductivity of Si anodes are resolved by this robust, hierarchical, and porous structure. As a result, the 3D Si anode realizes great performances in terms of Coulombic efficiency (>77.8% initial Coulombic efficiency), cycling stability (2381.8 mAh/g after 50 cycles at 0.1 C), and rate capability (1325.6 mAh/g at 2.1 A/g and 2624.9 mAh/g when returning to 0.42 A/g). Furthermore, artificial laponite's strong bonding ability and mechanical strength enable the creation of greater loading electrodes without fracture. Therefore, the Si anodes with the loading of 4–6 mg/cm^2 perform high areal/volume energy density and the lower capacity fade (*e.g.*, the capacity in the 4.34 mg/cm^2 is 4.7 mAh/cm^2 after 35 cycles). The advantages of this generic technique are straightforward and manageable, which can expedite the real application process of 3D Si anode.

Declaration of competing interest

The authors declare no competing financial interests.

Acknowledgments

This work was kindly supported by the National Natural Science Foundation of China (No. 51871113) and Natural Science Foundation of Jiangsu Province (No. BK20200047).

Supplementary materials

Supplementary material associated with this article can be found, in the online version, at doi:10.1016/j.cclet.2022.107946.

References

[1] K. Liu, Y. Liu, D. Lin, A. Pei, Y. Cui. Sci. Adv. 4 (2018) 9820.
[2] R. Zhan, X. Wang, Z. Chen, et al., Adv. Energy Mater. 11 (2021) 2101565.
[3] L. Zhang, X. Qin, S. Zhao, et al., Adv. Mater. 32 (2020) 1908445.
[4] Y. Liu, W. Li, Y. Xia. Electrochem. Energy Rev. 4 (2021) 447–472.
[5] S. Chae, M. Ko, K. Kim, K. Ahn, J. Cho, Joule 1 (2017) 47–60.
[6] S.A. Freunberger, Nat. Energy 2 (2017) 1–4.
[7] A. Kwade, W. Haselrieder, R. Leithoff, et al., Nat. Energy 3 (2018) 290–300.
[8] B.L. Ellis, W.R.M. Makahnouk, Y. Makimura, K. Toghill, L.F. Nazar, Nat. Mater. 6 (2007) 749–753.
[9] M.S. Dresselhaus, I.L. Thomas, Nature 414 (2001) 332–337.
[10] A. Huang, Y. Ma, J. Peng, et al., J. Energy Chem. 1 (2021) 141–162.
[11] T. Kennedy, M. Brandon, K.M. Ryan, Adv. Mater. 28 (2016) 5696–5704.
[12] C.M. Park, J.H. Kim, H. Kim, H.J. Sohn, Chem. Soc. Rev. 39 (2010) 3115–3141.
[13] Y. Son, J. Ma, N. Kim, et al., Adv. Energy Mater. 9 (2019) 1803480.
[14] X. Wang, G. Tan, Y. Bai, F. Wu, C. Wu, Electrochem. Energy Rev. 4 (2021) 35–66.
[15] S. Chae, S.H. Choi, N. Kim, J. Sung, J. Cho, Angew. Chem. Int. Ed. 59 (2020) 110–135.
[16] P. Li, G. Zhao, X. Zheng, et al., Energy Stor. Mater. 15 (2018) 422–446.
[17] A.N. Preman, H. Lee, J. Yoo, et al., J. Mater. Chem. A 8 (2020) 25548–25570.
[18] W. Luo, X. Chen, Y. Xia, et al., Adv. Energy Mater. 7 (2017) 1701083.
[19] L. Wei, Z. Hou, J. Mater. Chem. A 5 (2017) 22156–22162.
[20] G. Huang, J. Han, Z. Lu, et al., ACS Nano 14 (2020) 4374–4382.
[21] X.R. Wu, C.H. Yu, C.C. Li, Carbon 160 (2020) 255–264.
[22] S. Ye, L. Wang, F. Liu, P. Shi, Y. Yu, J. Energy Chem. 1 (2021) 75–82.
[23] C. Wei, H. Fei, Y. Tian, et al., Chin. Chem. Lett. 31 (2020) 980–983.
[24] J. Lee, J. Moon, S.A. Han, et al., ACS Nano 13 (2019) 9607–9619.
[25] C. Stetson, T. Yoon, J. Coyle, et al., Nano Energy 55 (2019) 477–485.
[26] J. Chang, X. Huang, G. Zhou, et al., Nano Energy 15 (2015) 679–687.
[27] H. Jiang, S. Wang, D. Shi, et al., J. Mater. Chem. A 9 (2021) 1134–1142.
[28] Y. Yan, X. Zhao, H. Dou, et al., Chin. Chem. Lett. 32 (2021) 910–913.
[29] B. Li, S. Yang, S. Li, B. Wang, J. Liu, Adv. Energy Mater. 5 (2015) 1500289.
[30] S. Jing, H. Jiang, Y. Hu, J. Shen, C. Li, Adv. Funct. Mater. 25 (2015) 5395–5401.
[31] N. Li, Y. Liu, X. Ji, et al., Chin. Chem.. Lett. 32 (2021) 3787–3792.
[32] Y. Zhang, C. Zhu, Y. Ye, F. Cheng, Energy Fuels 35 (2021) 18798–18804.
[33] P. Post, L. Wurlitzer, W. Maus-Friedrichs, A.P. Weber, Nanomaterials 8 (2018) 530.
[34] G. Zeng, Y. Liu, D. Chen, et al., Adv. Energy Mater. 11 (2021) 2102058.
[35] J. Labanda, J. Sabate, J. Llorens, Colloids Surf. A: Physicochem. Eng. Asp. 301 (2007) 8–15.
[36] S. Chae, Y. Xu, R. Yi, et al., Adv. Mater. 33 (2021) 2103095.
[37] L. Lin, Y. Ma, Q. Xie, et al., ACS Nano 11 (2017) 6893–6903.
[38] S. Yin, D. Zhao, Q. Ji, et al., ACS Nano 12 (2018) 861–875.
[39] Z. Liu, Q. Yu, Y. Zhao, et al., Chem. Soc. Rev. 48 (2019) 285–309.
[40] J. Ji, H. Ji, L.L. Zhang, et al., Adv. Mater. 25 (2013) 4673–4677.
[41] F. Zhang, G. Zhu, K. Wang, et al., J. Mater. Chem. A 7 (2019) 17426–17434.
[42] Z. Li, Y. Zhang, T. Liu, et al., Adv. Energy Mater. 10 (2020) 1903110.
[43] Z. Li, Y. Zhang, T. Liu, et al., Adv. Energy Mater. 10 (2020) 2000563.
[44] F.S. Li, Y.S. Wu, J. Chou, M. Winter, N.L. Wu, Adv. Mater. 27 (2015) 130–137.
[45] S.H. Park, P.J. King, R. Tian, et al., Nat. Energy 4 (2019) 560–567.